Materials Science and Engineering A 527 (2009) 305–316

Contents lists available at ScienceDirect

Materials Science and Engineering A

journal homepage: www.elsevier.com/locate/msea

Investigation of aluminum-based nanocomposites with ultra-high strength

Y. Li, Y.H. Zhao, V. Ortalan, W. Liu, Z.H. Zhang, R.G. Vogt, N.D. Browning, E.J. Lavernia, J.M. Schoenung*

Department of Chemical Engineering & Materials Science, University of California, Davis, CA 95616, USA

ARTICLE INFO

Article history:
Received 5 May 2009
Received in revised form 30 July 2009
Accepted 30 July 2009

Keywords:
Transmission electron microscopy (TEM)
Scanning transmission electron microscopy (STEM)
Aluminium alloys
Metal matrix composites (MMC)
Particulate-reinforced composites

ABSTRACT

Previously, we reported ultra-high compressive strength (up to 1065 MPa) for a bulk aluminum-based metal matrix nanocomposite [J. Ye, B.Q. Han, Z. Lee, B. Ahn, S.R. Nutt, J.M. Schoenung, Scr. Mater. 53 (2005) 481–486]. The mechanisms that are responsible for this significant strength increase over conventional materials (~225 MPa, H. Zhang, M.W. Chen, K.T. Ramesh, J. Ye, J.M. Schoenung, E.S.C. Chin, Mater. Sci. Eng. A: Struct. Mater. Prop. Microstruct. Process. 433 (2006) 70–82) and even over other equivalent nanocrystalline materials (~470 MPa, R.G. Vogt, Z. Zhang, T.D. Topping, E.J. Lavernia, J.M. Schoenung, J. Mater. Process. Technol., 209 (2009) 5046–5053) have not been studied in detail. The material consists of boron carbide reinforcement in a matrix with both coarse-grained and ultrafine-grained Al 5083; the processing introduces secondary phase dispersoids and dislocations. In this work, we systematically investigate the microstructural origins and the strengthening mechanisms, including Hall–Petch, Orowan and Taylor, as appropriate to each phase constituent. To provide insight into the relative contributions of these mechanisms, we calculate overall strength using rule-of-mixtures, modified shear-lag model, and Mori–Tanaka method.

1. Introduction

Particulate-reinforced metal matrix composites (MMCs) have the potential to provide tailored mechanical properties, for example, high specific stiffness and specific strength and creep resistance [1–3], which render them attractive for applications in the aerospace, defense and automotive industries to name a few [4–6]. Among the various MMCs, Al-based composites are of interest because of their low density and good formability [7,8]. These properties, in combination with recent interest in the high strength of nanostructured (NS) Al alloys [9–11] have prompted efforts aimed at using NS Al alloys as matrices in MMCs. These efforts have met with only limited success, partly as a result of the fact that the high strength in NS Al alloys is often accompanied with significantly diminished ductility [12–14]. A number of strategies have emerged in an effort to improve the poor ductility of NS materials [15–20]. In reference to these various strategies, numerous experiments have verified that the introduction of a bi/multi modal grain size distribution represents an effective approach to improve ductility while retaining a moderate strength level [17,21,22], because the NS microconstituent provides high strength while the coarse-grained (CG) microconstituent facilitates plasticity.

On the basis of these results, the novel concept of a tri-modal composite consisting of three phases: coarse-grained matrix, ultrafine- or nano-grained matrix and ceramic reinforcement was recently demonstrated [23]. B_4C was selected as the ceramic reinforcement, because it ranks third in hardness, just after diamond and cubic boron nitride, and possesses a low density of 2.51 g/cm^3 (which is even less than that of Al) [24]. Al 5083 was selected as a matrix material, given its importance in many applications [25]. This tri-modal composite, when tested in compression, exhibited extremely high strength (up to 1065 MPa), with a compressive strain-to-failure value of 0.8% [23]. Although the level of plasticity in this material is still quite low, it should be noted that without the addition of the coarse-grained material, the consolidated cryomilled Al 5083 plus B_4C failed in a brittle mode without any yielding [26]. Equivalent conventional and nanocrystalline materials exhibit significantly lower strengths (~225 MPa [27] and ~470 MPa [28], respectively), motivating the need to better understand the microstructural features that lead to this extremely high strength for an aluminum metal matrix composite.

There are two strengthening mechanisms that are typically associated with conventional MMCs: direct strengthening resulting from load transfer from the metal matrix to the reinforcing particle [29,30] and indirect strengthening resulting from the influence of reinforcement on matrix microstructure or deformation mode [31], such as dislocation strengthening induced by the deformation mismatch between the reinforcement and the matrix. In the case of the tri-modal composite, one needs to understand the individual roles of the UFG and CG microconstituents [29] and the accompanying grain refinement, Orowan (e.g., secondary phase dispersoids) and Taylor (dislocation based) strengthening mechanisms [32–35].

* Corresponding author.
E-mail address: jmschoenung@ucdavis.edu (J.M. Schoenung).

0921-5093/$ – see front matter © 2009 Elsevier B.V. All rights reserved.
doi:10.1016/j.msea.2009.07.067

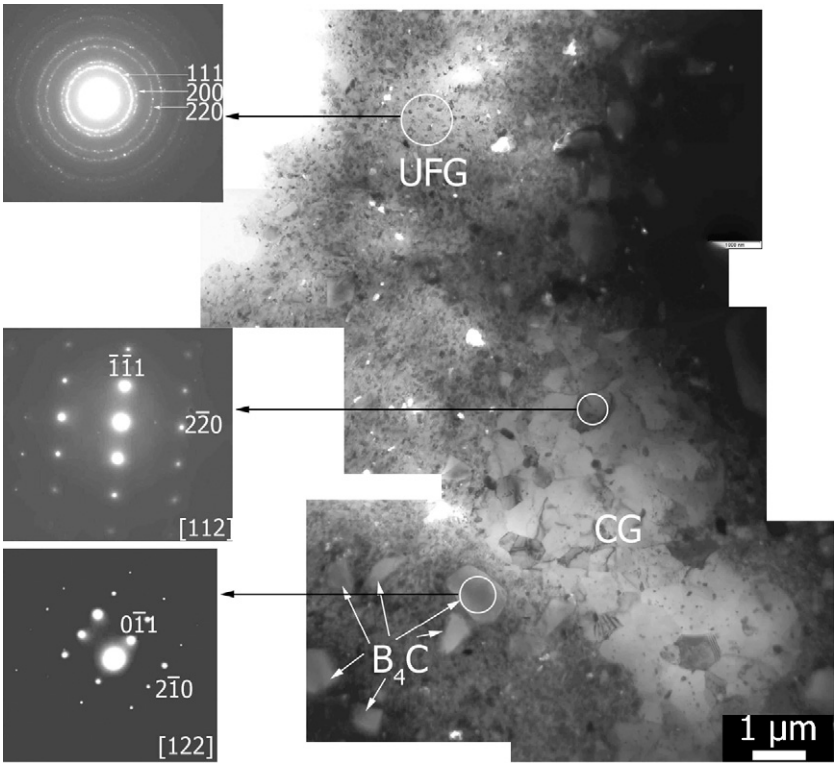

Fig. 1. The cursory distribution of coarse-grain (CG), ultrafine-grain (UFG) and B_4C microconstituents in the tri-modal Al 5083 based composite and their corresponding selected-area electron diffraction (SAED) patterns. The SAED patterns were obtained from the circle areas; the plane indexes and zone axis are marked in them.

Published results show that the strength of a tri-modal Al 5083 based composite, as calculated from the Hall–Petch relationship, and invoking an Orowan strengthening mechanism and the rule-of-mixtures, was 792 MPa [23], which is about 273 MPa lower than the experimental value. This discrepancy, in addition to the lack of published studies on this material, suggests that the microstructural origins of the strengthening behavior require further study.

In this work, we have performed systematic microstructure studies on the UFG and CG Al 5083 matrix in the tri-modal Al 5083 based composite specifically aimed at characterizing the following: (1) grain size and distribution, (2) composition and distribution of secondary phase dispersoids by scanning transmission electron microscopy (STEM) and energy dispersive X-ray spectroscopy (EDX), (3) dislocation density and configuration by high resolution electron microscopy (HREM), and (4) interface structures between

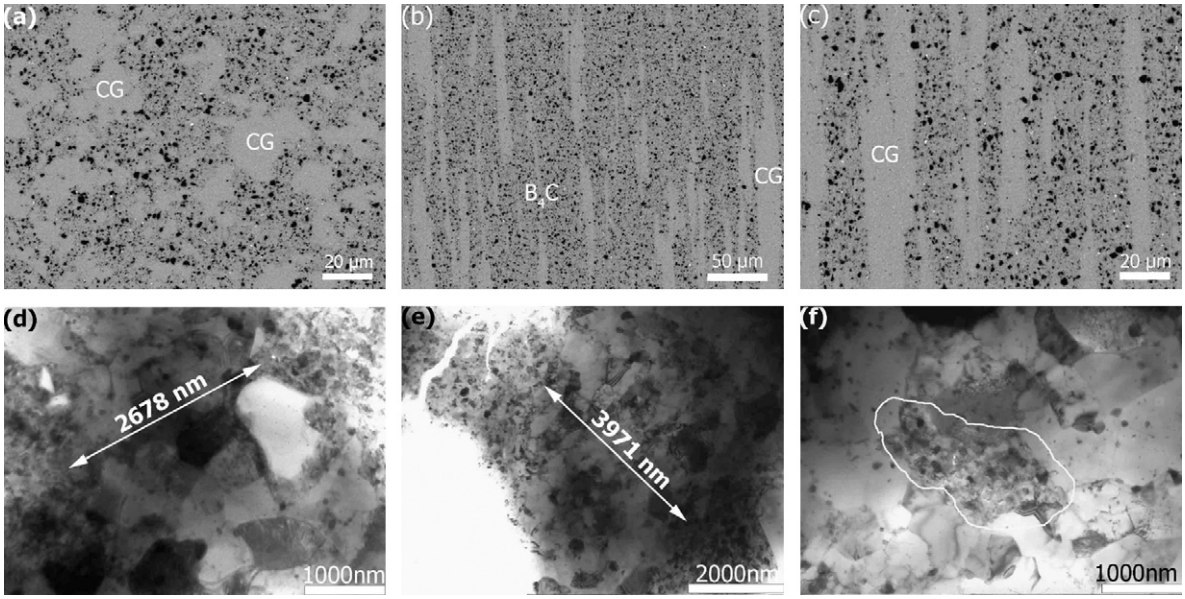

Fig. 2. Back-scattered electron images (BSE) showing the distribution of the UFG, CG, B_4C microconstituents in the tri-modal Al 5083 based composite from (a) top view and (b and c) side view; (d and e) TEM images showing the distance between two UFG regions; (f) an UFG region (encircled by white line) enclosed by CG regions.

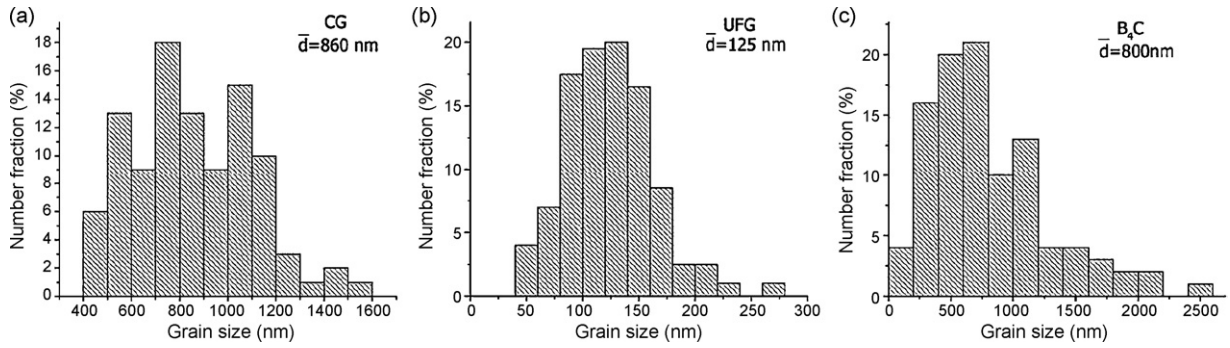

Fig. 3. Grain size histogram distributions for the (a) CG region, (b) UFG region and (c) B_4C particles in the tri-modal Al 5083 based composite, respectively.

the CG and UFG microconstituents and between the B_4C and the Al 5083 matrix. These factors are discussed in terms of the underlying microstructural mechanisms, and their possible contributions to the measured strength values.

2. Experimental

2.1. Sample preparation

The bulk tri-modal Al 5083 based composite was synthesized by cryomilling, blending, degassing, cold isostatic pressing (CIP) and hot extrusion, as described in previous studies [23,36,37].

2.2. Microstructural characterization

Scanning electron microscopy (SEM) images were taken in a Philips XL 30 FEG scanning electron microscope with a voltage of 15 kV. The TEM specimens were prepared by mechanically grinding the bulk materials to a thickness <30 μm, then dimpling from both sides to a thickness of approximately 10 μm. Further thinning to a thickness of electron transparency was carried out using a Gatan PIPS 691 ion milling system at a voltage of 4 kV. Low-magnification images and selected-area electron diffraction (SAED) patterns of the tri-modal sample were taken on a Philips CM12 transmission electron microscope at a voltage of 100 kV. A JEOL JEM 2500 SE transmission electron microscope operated at a voltage of 200 kV, equipped with high-angle-angular-dark-field (HAADF) detector, Gatan imaging-filter (GIF) energy dispersive X-ray spectroscopy (EDX) systems, was used for scanning transmission electron microscopy (STEM) imaging, composition analysis and HREM.

3. Results and discussion

3.1. Microconstituents identification and distribution

The UFG, CG and B_4C microconstituents in the Al 5083 based composite were revealed by bright-field TEM imaging, as shown in Fig. 1. The B_4C particles, primarily distributed within the UFG regions, have an angular morphology containing straight and sharp interfaces with the Al 5083 matrix. The morphology of the B_4C particles is consistent with that of the starting powder. The B_4C particles were enclosed in NC Al 5083 powder during cryomilling and therefore had no direct contact with the CG powder during subsequent blending and consolidation procedures. The inserts in Fig. 1 are the SAED patterns from the areas indicated by circles for UFG, CG and B_4C microconstituents, respectively. The SAED ring of the UFG region indicates a random crystal orientation of the UFG grains. The SAED of the B_4C confirms the hcp structure from which the calculated lattice parameter is consistent with the JCPDS card (75-0424).

Details on the distributions of the three microconstituents were further characterized by SEM and TEM, as shown in Fig. 2. Fig. 2(a) is an SEM image from a planar view of the extruded sample (perpendicular to the extrusion direction), and Fig. 2(b and c) are SEM images from the cross-sectional view of the sample (parallel to the extrusion direction). In Fig. 2(a–c), the black particles are B_4C, the gray regions free of B_4C are CG regions, and the gray regions with B_4C particles are the UFG regions. From Fig. 2(a), one can see the UFG regions with B_4C particles are uniformly distributed at the boundaries of the spherical CG regions. Alternatively, one can describe the CG microconstituent as being separated by the UFG regions in the plane vertical to the extrusion direction. Fig. 2(b and c) reveals the elongated CGs originated from the extrusion. Fig. 2(a–c) also shows that the B_4C particles are uniformly distributed in the UFG region with an average particle distance of about 3–4 μm. Since the CG agglomerates were separated by the UFG regions, the distance between two neighboring UFG regions is the size of CG agglomerates, which was calculated to be approximately 3–4 μm on the basis of a large number of bright-field TEM observations, a representative image of which is shown in Fig. 2(d and e). Similarly, the distance between two CG agglomerates is the size of the B_4C and UFG region, which is approximately 10 μm as measured from the SEM images. The distance between two CG regions was not measured from TEM images because it is beyond the thin area of the TEM specimens. Fig. 2(f) shows an occurrence of a small UFG region with a length of about 1 μm, which was enclosed by the CG regions.

3.2. Grain sizes of UFG and CG microconstituents and B_4C particle size, and their distributions

From TEM images and SEM images, we statistically measured the grain/particle size distributions of the UFG, CG and B_4C microconstituents, as shown in Fig. 3(a–c). One can see that the grain/particle sizes of CG, UFG and B_4C microconstituents varied from 700 to 1200, 80 to 160 and 500 to 1500 nm, respectively. On the basis of the formula for average grain size, $A = S_aN_a + S_bN_b + \ldots + S_iN_i + \ldots$ (where A is the average grain size, S_i is the grain size within a narrow range, N_i is the concentration of grains of size S_i), the average grain/particle sizes of CG, UFG and B_4C were estimated as 860, 125 and 800 nm, respectively. On the basis of the definition of UFG materials (with grain size smaller than 1 μm and larger than 100 nm), the CG region also has UFG grains, however, in this work we retained the original designation of CG given its origin from the unmilled Al 5083 powder.

3.3. Secondary phase dispersoids and their distribution

Different from diffraction contrast, the HAADF mode (STEM) provides incoherent images and uses high-angle scattering and therefore leads to strong atomic number (Z) contrast [38]. The

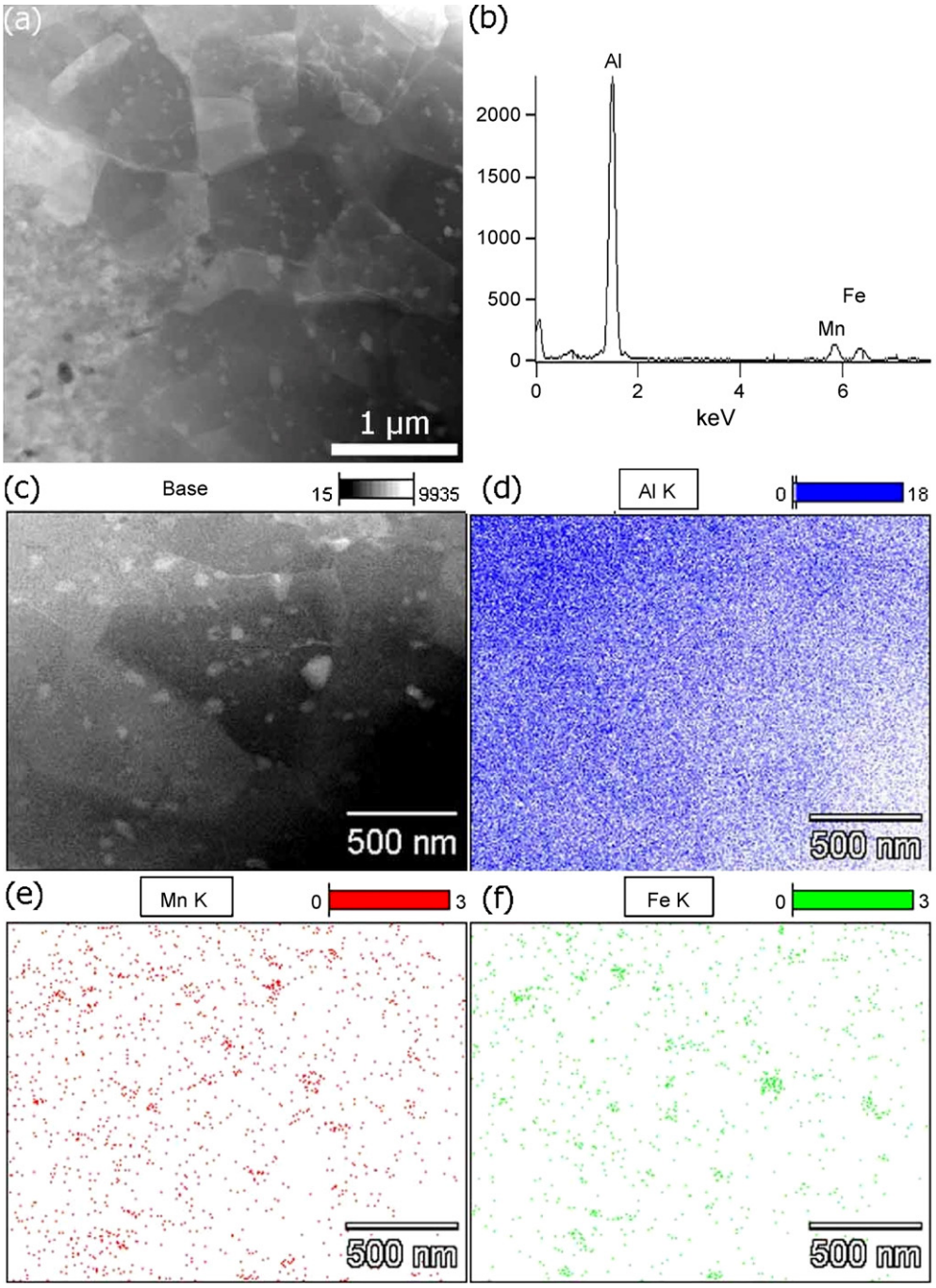

Fig. 4. (a) STEM image revealing the distribution of the secondary phase particles in the CG region of the tri-modal Al 5083 based composite, (b) the typical EDX result from the secondary phase particles in the CG region, (c) Base image for EDX mapping in partial CG region, and EDX elements mapping of same region for (d) Al, (e) Mn and (f) Fe, respectively.

intensity of the atom columns is approximately proportional to the mean square of the atomic number; and as such, the contrast in such a mode is strongly dependent on chemical composition [39]. Fig. 4(a) presents a low-magnification HAADF image of a CG region. The CG grains and grain boundaries can be clearly seen with numerous white dispersoids (with a diameter/length of about 50 nm). The white color, i.e., intense scattering from the dispersoids, suggests that they consist of high atomic number elements. EDX point scan results, which were generated from more than 10 dispersoids, a representative spectrum of which is shown in Fig. 4(b), indicate that the dispersoids include Al, Mn and Fe elements. To verify this further, EDX element mapping analysis was conducted in a local region as shown in Fig. 4(c–f). Fig. 4(c), which is the base image of the local region used for the EDX mapping in Fig. 4(d–f), shows the corresponding Al, Mn and Fe element mapping in the same region as Fig. 4(c). Apparently, Al is evenly distributed throughout the entire region; the color gradient from left to right is ascribed to a change in thickness. From Fig. 4(e and f), we can see that most of the elemental Fe and Mn are mostly associated with the white dispersoids. These dispersoids originate from the composition of the Al 5083. Table 1 lists the chemical analysis results for the tri-modal Al 5083 based composite (performed by Luvak Inc.). Elemental Fe, Mn represents the third and fourth highest concentrations, respectively, after Al and Mg. On the basis of published studies, the most likely

Table 1
The chemical analysis results for the tri-modal Al 5083 based composite (provided by Luvak Inc.).

Elements	Mg	Mn	Fe	Cr	H	O	N
Concentration (wt.%)	4.59	0.62	0.54	0.15	0.0114	1.62	0.72

phase for the dispersoids is Al_6(Mn,Fe) [40], which agrees with our EDX mapping analyses. In addition, we also did the EDX mapping for elemental Mg, Cr in the area of Fig. 4(c), but did not find any enrichment areas. The average distance between two secondary phase dispersoids, as estimated from Fig. 4(a), is approximately 300 nm.

In addition to the above results from the CG area, we also performed low-magnification STEM in the UFG region, as shown in Fig. 5(a), where the dispersoids are marked by arrows. One can see the majority of the dispersoids were located at the grain boundaries. EDX composition point analyses were conducted for all of these dispersoids. Fig. 5(b) represents a typical EDX spectrum, from which one can see that there are Al, Mn and Fe peaks, indicating that the main dispersoids in the UFG region are the same as those in the CG region, i.e., Al_6(Mn,Fe). In addition to the Al_6(Mn,Fe) dispersoids, in the UFG region we also observed a few dispersoids that contain other elements. Fig. 5(c) presents a corresponding EDX result for a large dispersoid with a size larger than 200 nm (marked by "C" in Fig. 6(a)). In addition to Mn and Fe, the dispersoid is also enriched in Cr and Cu. Moreover, the average distance between two dispersoids is the same as that in the CG region. In addition to the grain boundaries, dispersoids were also observed in the grain interiors, as shown in Fig. 5(d). Two large dispersoids are denoted by black arrows. The composition of the dispersoids inside the grains is still Al_6(Mn,Fe) as verified by EDX analysis. The STEM imaging and EDX analysis were also carried out at the interface between the B_4C particles and the UFG region, and no obvious elemental segregation was observed.

3.4. Dislocation structure and geometry

Dislocation structures in both UFG and CG regions were studied by large-area TEM observations. Fig. 6(a) is a low-magnification TEM image of the CG region showing dislocations arranged in various geometries, such as dislocation networks (Fig. 6(b)), tangling of multiple dislocations at grain interiors (Fig. 6(c)), polygonized dislocation walls that form subgrain boundaries (Fig. 6(d)) [41], tangling of dislocations inside a coarse grain (Fig. 6(e)), a subgrain boundary formed by dislocation re-arrangement (Fig. 6(e)), and several relatively straight dislocations in one coarse grain (Fig. 6(f)). Moreover, it is apparent that a majority of the dislocation line directions are not the same, suggesting that these dislocations are mixed dislocations consisting of pure edge dislocations and pure screw dislocations. The semi-circle dislocation structure (marked by an arrow in Fig. 6(f)) also verifies this suggestion. Noteworthy is the fact that we observed a very low density of dislocations in

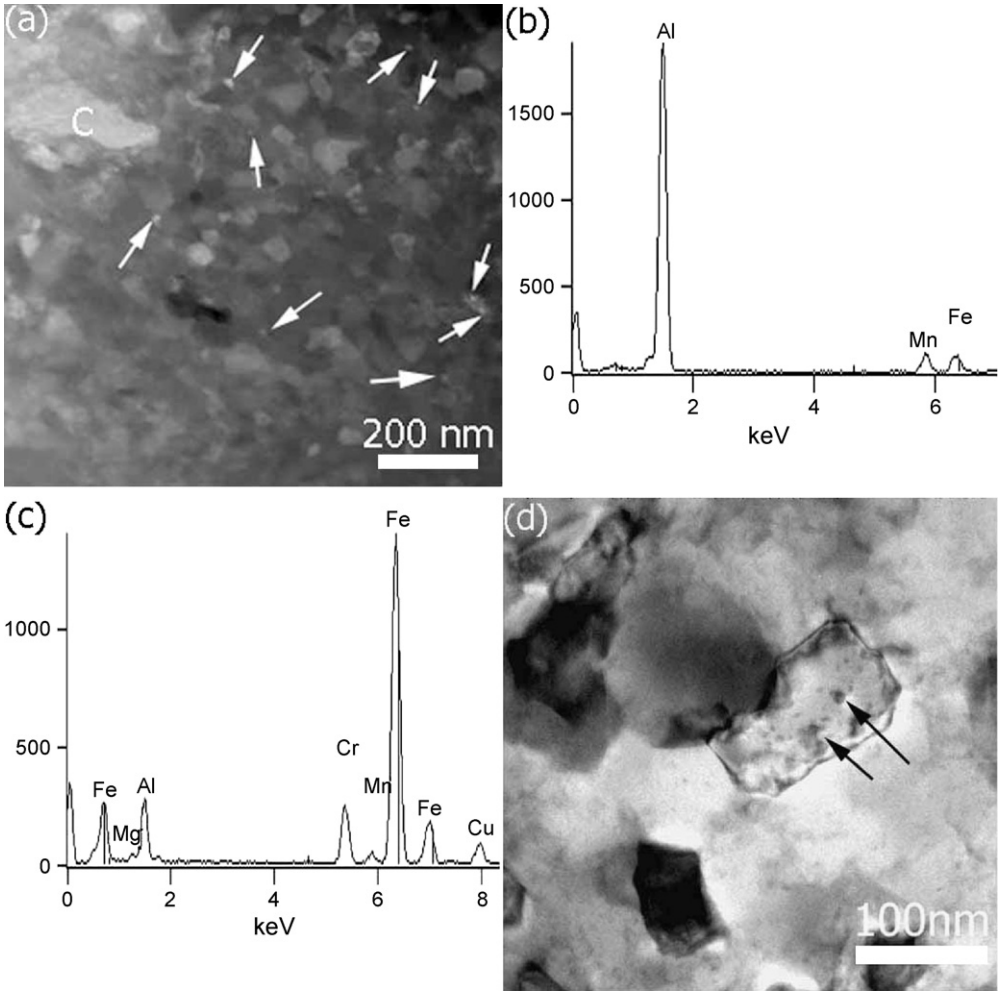

Fig. 5. (a) STEM image showing the distribution of the secondary phase particles (marked by white arrows) in the UFG region of the tri-modal Al 5083 based composite. (b) Typical EDX spectrum from the main precipitates in Fig. 5(a), (c) EDX spectrum from the larger precipitate, which is marked by "C" in Fig. 5(a), (d) TEM bright-field image of UFG region showing a high-density of secondary phase particles in the grain interior.

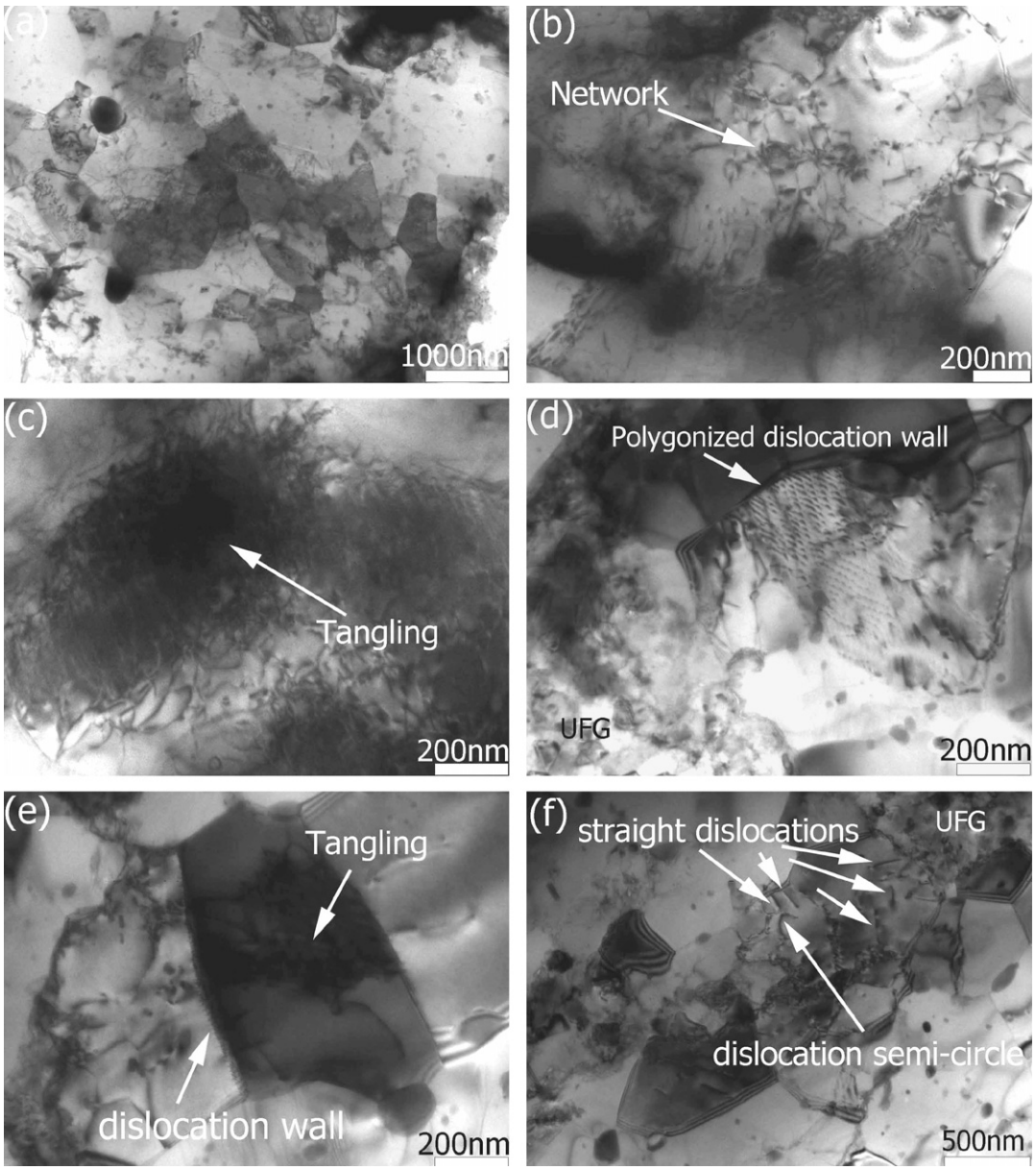

Fig. 6. (a) High-density dislocation structures distributed in the CG region, (b) partial dislocations network, (c) tangled dislocations, (d) high-density dislocation wall (marked by white arrow), (e) a subgrain boundary formed by dislocation re-arrangement (marked by arrow) and dislocation tangling, (f) dislocation semi-circle and straight dislocations line in the CG region.

the UFG region as compared with in the CG region. This observation can be rationalized as follows. It is difficult for the UFG grains to contain dislocation forest/tangling because when the grain size is below a critical value, the mean free path of dislocations was limited only by its grain boundaries [41]. Moreover, the final extrusion step is likely to have promoted large plastic deformation in the CG regions leading to a high-density of dislocations. The few dislocations observed in the UFG regions are also believed to be introduced during the final hot extrusion. The reason for this is that the UFG regions originate from the cryomilled Al 5083 powders, which, for our case, the grain size of the cyomilled powders was about 25 nm. The UFG regions (with an average grain size of 125 nm) result from the grain growth of the cryomilled Al 5083 powders during the degassing process (500 °C). The initial nanocrystalline powder should contain a very low concentration of dislocations because of the very fine grain size. Even if there are some dislocations in the initial nanocrystalline grains, they should be annihilated by the recovery process during grain growth. Thus, the dislocations form during the extrusion process, yet, the small UFG grains limit the formation of dislocations. In addition, the extrusion process is carried out at a temperature of 525 °C, during which some annealing should take place, which would again annihilate dislocations. The final result is that very few dislocations remain in the UFG region of our tri-modal Al 5083 composite.

The accumulation of a high-density of dislocations in the CG region is believed to play an important role in determining the strength of the CG microconstituent and therefore the overall strength; hence, we measured dislocation density in the CG regions by HREM methods [42], as shown in Fig. 7(a). Fig. 7(b) is the corresponding inverse Fast Fourier Transformation (FFT) pattern of (a), in which the edge dislocations structures are marked by "T". The dislocation density present in the CG regions, calculated on the basis of statistical dislocation numbers obtained from tens of

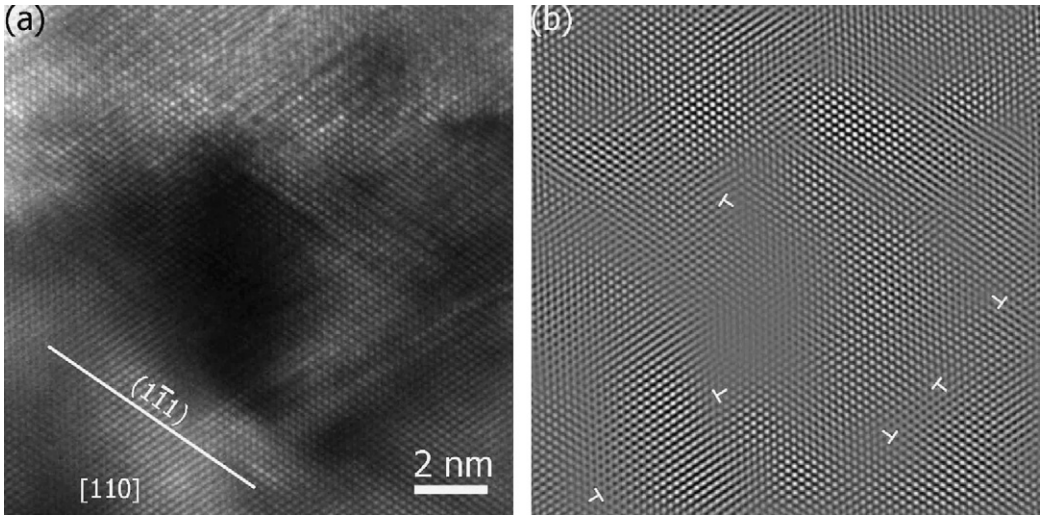

Fig. 7. (a) HREM image taken from the CG region, with [1 1 0] zone axis, (b) Inversed Fast Fourier transformation pattern of the image in (a), where dislocation cores were marked by "T".

HREM images, is $4.5 \times 10^{14}/m^2$. It is noted that dislocation density can also be measured by several techniques, including X-ray peak broadening method [11,43] and electrical resistivity techniques [44]. However, for the current composite material, HREM provides a direct measurement of the dislocation density in the CG regions.

3.5. Interface structure

To provide insight into the role of interfaces on the mechanical behavior, we selected two primary regions for detailed TEM examination, the UFG/CG Al 5083 and B_4C/Al 5083 interfaces. Fig. 8(a) shows a lower magnification bright-field TEM image from the

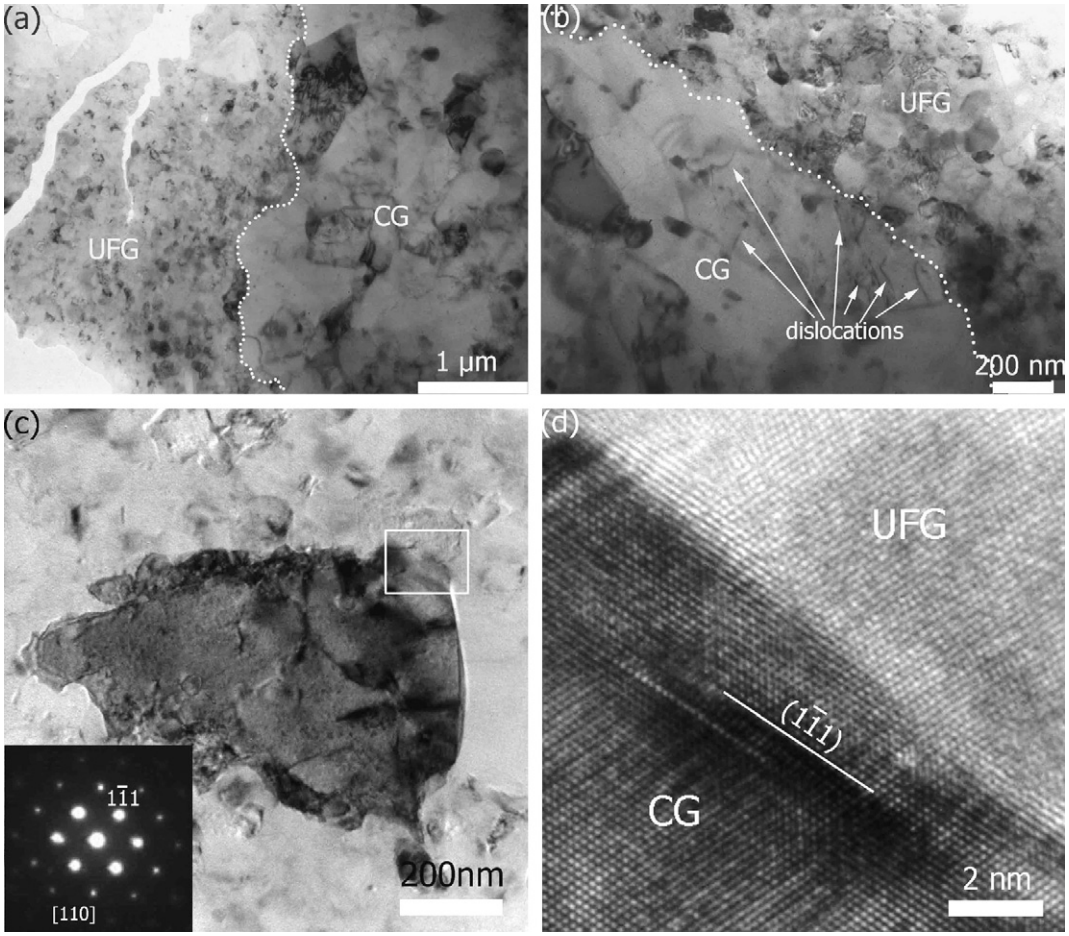

Fig. 8. (a and b) Bright-field images with different magnification of the interface between the UFG region and the CG region, (c) bright-field image showing a coarse grain and corresponding SAED patterns with [1 1 0] zone axis, (d) HREM image of the partial area that is enclosed by the rectangle in (c), showing the UFG/CG interface is metallurgically clean.

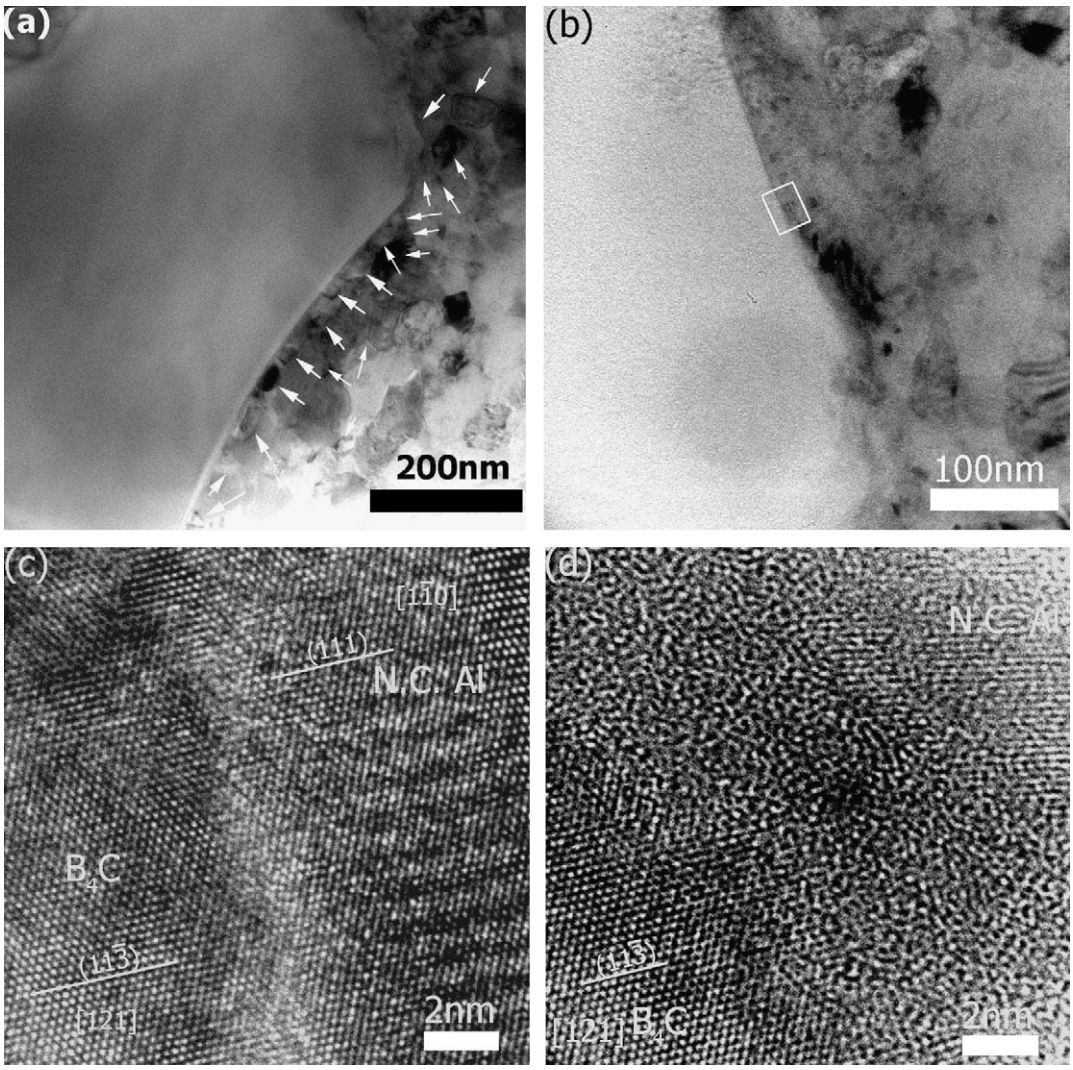

Fig. 9. (a) STEM image of the B_4C/UFG interface showing 2–3 layers of nanocrystalline (NC) Al 5083 (marked by arrows) formed at the interface, (b) TEM bright-field image of B_4C/UFG interface showing the existence of NC layers, (c) HREM image from the area enclosed by a rectangle in (b) showing the B_4C lattice linked with Al 5083 matrix directly, (d) HREM image of B_4C/UFG interface showing a 5–8 nm amorphous buffer layer between the B_4C particles and the NC Al 5083 matrix.

UFG/CG interface, which is highlighted with a discontinuous white line. A portion of the UFG/CG interface in Fig. 8(a) is magnified in Fig. 8(b), from which we can see that a lamellar CG is linked with many UFGs. A few dislocations, which appear to be pinned near the interface, are present at the interface of the UFG and CG regions. Fig. 8(c) shows a large coarse grain surrounded by UFG grains, and the inset is the corresponding SAED pattern. The interfacial region in the square in Fig. 8(c) is magnified in Fig. 8(d). In this figure it is evident that the Al lattice of the coarse grain are directly linked with the lattices of the ultrafine grains.

In addition to the UFG/CG interfaces, we also studied the B_4C/UFG interfaces. One interesting phenomenon is that almost all of the B_4C particles were enclosed by 2–3 layers of nanocrystalline (NC) Al 5083 grains with a size <50 nm, as shown in Fig. 9(a). It is worth noting that this NC layer has an average grain size of 35 nm, which is smaller than the average grain size of the UFG region (125 nm). Assuming that the B_4C geometry can be approximated by a cube with a length of 800 nm and that each particle is enclosed by two NC layers, the volume of the NC layer surrounding a B_4C particle can be calculated as $(870^3–800^3)\,nm^3 = 1.5 \times 10^8\,nm^3$, and thus the volume fraction of the NC layers can be estimated as $(1.5 \times 10^8\,nm^3/800^3\,nm^3) \times 10\% = 3\%$. Although the mechanisms that are responsible for the formation of the NC layers are still under investigation, they are likely associated with the cryomilling process given that the Al 5083 surrounding the B_4C particles is likely to experience a high strain during milling.

Fig. 9(a and b) shows the absence of discontinuities or voids at the B_4C/UFG interface. Fig. 9(c and d) are HREM images from the region that is enclosed by a rectangle in Fig. 9(b). Two types of B_4C/UFG interfaces were observed and are described as follows. In one type of interface, a B_4C particle is in intimate contact with the Al 5083 lattice and no intermediate layers or defects are evident at this interface (Fig. 9c). The Moiré fringe structure that is evident in the NC Al 5083 region is thought to arise from the misorientation from two overlapped NC Al 5083 grains. In the second type of B_4C/UFG interface a transitional amorphous layer is evident, as shown in Fig. 9(d). The width of this amorphous layer is estimated to be as large as 5–8 nm. The former type of interface, which is the one most commonly observed, may be formed in cases where there is no large lattice mismatch between B_4C and NC Al 5083, whereas the latter type, which is only rarely observed, might be caused by a large lattice mismatch at the interface. The amorphous layer is likely to have formed to lower the large lattice mismatch energy [45]. The amorphous layer is thought to originate from the Al_2O_3 that is present at the surface of the Al 5083 grains [46] or possibly from amorphitization during the inter-diffusion between

Table 2
Density, initial yield strength and elastic modulus of the main microconstituents in the tri-modal Al 5083 based composite [27,49].

Item	Density (g/cm^3)	Strength (MPa)	Elastic modulus (GPa)
Coarse-grained Al 5083	2.657	124	70
B_4C particles	2.51	2900	448

Table 3
Microstructures of the UFG, CG and NC microconstituents in the tri-modal Al 5083 based composite.

Item	CG	UFG	NC
Grain size (nm)	860	125	35
Average spacing of grain region (μm)	10–20	3–4	N/A
Size of secondary phase particles (nm)	30–50	20–30 at grain boundary, 5–15 at the grain interior	N/A
Average spacing of secondary phase particles (nm)	200	200	N/A
Dislocation density (m^{-2})	4.5×10^{14}	N/A	0

B_4C and Al during degassing and hot extrusion [45]; work aimed at elucidating this phenomenon is continuing.

4. Microstructure contributions to strength

The above results provide systematic information on the various microstructural microconstituents of the tri-modal composite, the results of which are summarized in Table 3. In the sections that follow we use this information to provide insight into the relative contributions of individual strengthening mechanisms, on the basis of available theories. We then look at select approaches to aggregate the strength contributions so that overall strength can be estimated.

4.1. Grain refinement

The strengthening brought about by grain refinement can be described by the Hall–Petch relationship $\sigma_y = \sigma_0 + K_y/\sqrt{d}$, where σ_y is the final strength value after considering the effect of grain size, σ_0 is the initial strength value, K_y is a constant and d is the mean grain size [47,48]. Here, the K_y value was chosen as 0.22 MPa$\sqrt{m}$, on the basis of published studies by Last and Garrett in which they calculated the strength of a mechanically milled Al–7.5%Mg alloy [49], with a σ_0 of 124 MPa [50]. Using the initial strength value and grain sizes listed in Tables 2 and 3, values of σ_y for the CG, UFG and NC Al 5083 were calculated to be 360 MPa, 750 MPa and 1300 MPa, respectively, as listed in Table 4.

4.2. Orowan strengthening

Dispersoid strengthening can be estimated on the basis of the Orowan strengthening mechanism: $\sigma_{or} = (0.4Gb/\pi(1-\nu)^{1/2})(\ln(\bar{d}/b)/\bar{\lambda})$, where M is the mean orientation factor for face-centered cubic Al (3.06), G is the shear modulus (25.9 GPa), b is the Burgers vector (0.286 nm), ν is the Poisson's ratio (0.33), $\bar{d}$ is equal to $\sqrt{2/3}d$ and $\bar{\lambda}$ is equal to $(\bar{d}(\sqrt{\pi/4f} - 1))$, where f is the concentration of the secondary phase dispersoids in the material [51]. Statistical analysis of the microstructures shows that the diameters of dispersoids in the grain interior of the UFG and CG regions are 5–15 and 30–50 nm, respectively, and hence we used average values of 10 and 40 nm, respectively, for the calculations. The density of dispersoids was estimated on the basis of 40 STEM images to be nominally 16 secondary phase dispersoids in one coarse grain. If we assume this coarse grain to have a cubic morphology, with a volume that can be estimated as 860^3 nm^3, the volume of secondary phase dispersoids can then be estimated as 16 nm × 6 nm × 40^3 nm, hence the concentration is (16 nm × 6 nm × 40^3 nm)/(860^3 nm^3) = 1%. In view of the fact that the concentration of dispersoids in the UFG region is similar to that in this coarse grain we assume the value of 0.5%, consistent with that in the literature [52]. Thus the strength contributions originating from secondary phase dispersoids in the CG and UFG regions can be estimated to be 50 MPa and 125 MPa, respectively.

4.3. Taylor relationship

The dislocation density contribution to the strength can be calculated on the basis of the Taylor formula $\tau = CGb\sqrt{P}$ [53], where P is the density of dislocations, G is the shear modulus (25.9 GPa), b is the magnitude of the Burger's vector (0.286 nm) and C is a constant assumed to be 0.3 by Ashby [54]. According to this formula, the shear strength of the CG region that is associated with dislocations can be calculated to be τ = 45 MPa. By using $\sigma = 3.1\tau$ [55], the overall contribution to yield strength from the dislocation structures present in the CG regions can be estimated to be 140 MPa.

4.4. Overall strengthening behavior based on available models

Recognizing that interactions amongst the various strengthening mechanisms described above are likely to be complex, the select models employed here to aggregate the strength contributions into an overall strength are intended to provide insight as to whether the studied mechanisms can, within a reasonable range of certainty, be highlighted as the mechanisms that do indeed lead to the ultra-high strength exhibited in this material. It is therefore noted that the models described below should be considered as merely providing bounds to the overall behavior. Nevertheless, the calculations do provide insight into the relative contributions of each mechanism.

Beginning with an aggregation of strengthening mechanisms within a given microconstituent, a simple summation is applied. Summing the contributions from grain size, secondary phase dispersoid and dislocation strengthening, shown in Table 4, results in an overall estimated strength of 550 MPa for the CG region, 875 MPa for the UFG region, and 1300 MPa in the NC region. The inherent strength of the B_4C particles is estimated as 2900 MPa [24]. The relative strengths associated with the CG and UFG regions were further confirmed through microhardness testing. Vickers microhardness values for these two regions (using a test load of 25 g) are 120 HV and 270 HV, respectively; this trend is consistent with the above results, given the inherent uncertainty associated with both the microhardness test and the strength approximation methods.

In order to aggregate the microconstituents and thereby estimate the overall strength of this particulate-reinforced composite, three established models are employed: (1) rule-of-mixtures, (2) the modified shear-lag model, and (3) the Mori–Tanaka approach.

Table 4
Microstructural contributions to strength for the CG, UFG, and NC microconstituents in the tri-modal Al 5083 based composite.

Strengthening mechanism	CG (MPa)	UFG (MPa)	NC (MPa)
Original strength	124	124	124
Grain size (includes original strength)	360	750	1300
Secondary phase particles	50	125	–
Dislocations	140	–	–
Sum	550	875	1300

4.4.1. Rule-of-mixtures

In the particular case of fiber-reinforced composite materials there is considerable evidence to support a so-called "rule-of-mixtures" for calculating the tensile strength of a composite that fails, at a strain below the final failure strain of the matrix [56]. The rule-of-mixtures has also been used to estimate the strength of fiber-reinforced cements, metal matrix dual-phase nanocomposites and particle reinforced composites [56–58]. The rule-of-mixtures provides perhaps the simplest approach, based on a volume fraction weighted strengthening. It is important to note that this simple linear combination of values fails to take into account the plastic behavior of the matrix, as well as the inelastic response of the ceramic phase [59–61]. In this case, $\sigma = \sigma_m(1-f)+\sigma_r f$ [56], where f is the volume fraction, σ_m is the strength of the matrix, and σ_r is the strength of the reinforcement phase. Because of the similar density values for Al 5083 and B_4C (Table 2), the weight fractions of the various microconstituents in the tri-modal Al 5083 based composite can be approximated as volume fraction. The results of this weighted summation estimate the strength of the tri-modal Al 5083 based composite to be 930 MPa, which compares relatively well with the measured strength value (~1065 MPa).

4.4.2. Modified shear-lag model

The modified shear-lag theory [1] provides a model of strengthening that employs a modification to the conventional shear-lag theory [1,62] by using equations developed for predicting discontinuous composite strength because of load transferred by shear [63], and incorporates a term to account for tensile stress transfer occurring at the reinforcement ends. An assumption is made that the presence of the reinforcement does not affect the matrix stress–strain behavior, which allows the properties of the matrix to be incorporated into the model. It should also be noted that the modified shear-lag theory assumes that a strong bond exists between the matrix and reinforcement, which has been confirmed experimentally [64]. The modified shear-lag model can be written as: $\sigma = \sigma_m[1/2V_r(s+2)+V_m]$ [1], where σ is overall strength of the composite, σ_m is the strength of the matrix, V_r and V_m are the volume fraction of the reinforcement phase and matrix, respectively, and s is the aspect ratio of the reinforcement phase (the ratio of length vs width of the reinforcement phase particle). In this study we assume an aspect ratio of 1, and if we consider the coarse-grain microconstituent as the matrix, and the others as reinforcement, the strength of the tri-modal Al 5083 based composite can be estimated as 688 MPa. If we consider the UFG region as the matrix, the strength of the tri-modal Al 5083 is estimated to be 1138 MPa. Because the volume fraction of UFG region is approximately equal to that of the CG region, it is reasonable to average these two values. The average estimated strength, using the modified shear-lag model is therefore 915 MPa, a value that is similar to the results obtained using a simple rule-of-mixtures.

4.4.3. Mori–Tanaka method

The Mori–Tanaka method is an approach that uses an explicit analytical expression based on the Mori–Tanaka (M–T) mean-field concept [65]. This approach is relatively simple (compared with finite unit calculation) and can predict the mechanical response over an entire range of the inclusion shapes and volume fractions. Weng presented a modified version of the theory [66], the secant approach, which allows the elasto-plastic representation of both phases. In this case the two phases are represented in a matrix-inclusion topology and the secant approach models the weakening constraint of the matrix as the macroscopic stress or strain increases. The method has shown promise in predicting the stress–strain behavior of dual-phase steels and metal matrix composites with elastic inclusions [66–68]. Joshi et al. proposed an approach based on the secant M–T method to describe the overall response of hierarchiacal composites with each of many phases deforming elasto-plastically [69,70]. They used the Voce equation instead of the Ludwig equation to describe the mechanical behavior [66], as it better represents the overall flow behavior of the materials. Here we use the same code and program as they used in order to combine our strength values from the main microconstituents and thereby describe the overall response of the tri-modal Al 5083 based composite. Similar to the assumptions made by Joshi et al., we consider the UFG region, including the B_4C particles, as an inclusion phase or level-I composite, then the level-I composite is considered to be the inclusion phase within the CG region to comprise the level-II composite. Because the simulation parameters for the 3% NC grains are not available, we consider them to be UFG grains. From the M–T method, we first establish the overall response of the level-I composite, and then we fit it by using a Voce equation in order to obtain the parameters required for calculation of the level-II composite behavior. Once these two steps are completed, we can then predict the overall response for the tri-modal Al 5083 based composite. The Voce equation is defined as [71],

$$\sigma = \sigma_s - (\sigma_s - \sigma_y)e^{(-\varepsilon_p/\varepsilon_c)}$$

where σ, σ_y, σ_s, ε_p, and ε_c are practical yield stress, the initial yield stress, saturation stress, plastic strain, and the characteristic strain, respectively, for the phase in the composite. With the exception of the initial yield stress for the UFG region (we use our value of 875 MPa), the other parameters are assumed to be the same as those reported by Joshi et. al. for the level-I composite. In the case of the parameters of the level-II composite, we use our initial strength value for the CG microconstituent, which is 550 MPa. The parameters of the level-I composite were obtained by fitting the stress–strain curves (the fitted parameters are σ_y = 1096 MPa, ε_c = 0.0167, σ_s = 1439 MPa). The overall response of the tri-modal composite is shown in Fig. 10. From this figure, the overall strength of the tri-modal Al 5083 based composite can be estimated to be approximately 855 MPa, which is lower than the experimentally determined value.

4.4.4. Microstructure control

The results obtained using the abovementioned models (930 MPa, 915 MPa, 855 MPa) indicate that regardless of aggregation method, it is reasonable to state that the microstructural features characterized in this in-depth analysis are responsible for the vast majority of the strengthening observed in this material (~1065 MPa). The results further indicate that there are some other

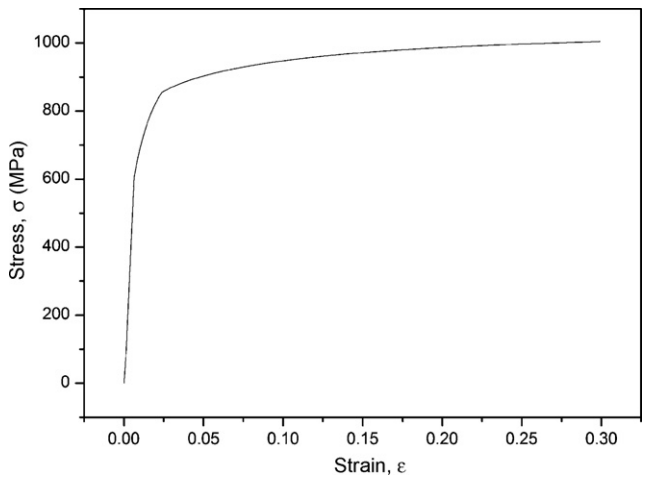

Fig. 10. The computed overall stress (σ)–strain (ε) responses using the Mori–Tanaka method.

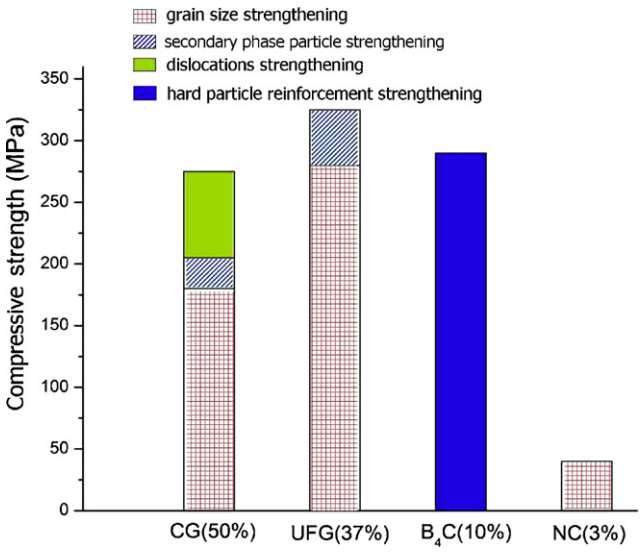

Fig. 11. Histogram showing the contributions of the four microconstituents and various strengthening mechanisms to strength of tri-modal Al 5083 based composite. (Volume percents in parentheses.)

factors that need to be taken into consideration. For example, the role of impurities, such as H, N and O, which are well known to influence mechanical response are absent in the above calculations. The presence of N and O may lead to the formation of nano-sized AlN and Al_2O_3 particles (on the basis of their thermodynamic stability), respectively, which can further increase the yield strength through Orowan strengthening and/or hard particle strengthening, depending on their size and distribution [72–74]. The presence of H is, on the other hand, detrimental, as it can lead to embrittlement [75]. A key purpose of the degassing step is to minimize the H content. Further investigation is ongoing to fully characterize the location and distribution of these phases and their contribution to the strength of this material, although their extremely fine scale will render any quantitative analysis challenging.

In an effort to utilize the numerical approximations to provide further insight into the various strengthening mechanisms investigated in this study, the results originating from the rule-of-mixture approximation are presented graphically in Fig. 11. It is interesting to note that the NC region, although representing only 3% by volume, contributes almost 4.5% of the strength. Furthermore, for all microconstituents, other than the B_4C particles of course, grain size strengthening is the dominant mechanism, followed by dislocation strengthening and then secondary phase strengthening. In evaluating these results it is important to note that, although volume fraction can be fairly easily modified through process modification, control of the other parameters can be more challenging, yet more important. For instance, the grain size is influenced by the thermal exposure during each of the powder processing and consolidation steps, especially in degassing and hot extrusion. The formation of secondary phase dispersoids, their concentration, distribution and relative size, is controlled by cryomilling, degassing, and hot extrusion. The density of dislocations is strongly influenced by the degree of deformation that occurs during consolidation, especially extrusion in our case. Furthermore, the role of the clean interfaces between the microconstituents to effectively permit load transfer, which derive from the cryomilling and blending, cannot be overlooked.

5. Summary

In this work, an in-depth microstructural analysis was coupled with existing mechanics models to quantitatively and qualitatively examine a bulk tri-modal Al 5083 based composite and the likely mechanisms that govern its strengthening behavior. The results may be summarized as follows.

1. In addition to Hall–Petch strengthening in the CG and UFG Al 5083 matrix, we also found dispersoids and dislocations, which further increase the strengths of the UFG and CG microconstituents to about 875 MPa and 550 MPa, respectively.
2. The B_4C particles were enclosed by a thin nanocrystalline Al 5083 layer with an average grain size of approximately 35 nm and a volume fraction of ~3%. Using Hall–Petch strengthening as the basis, the strength of this microconstituent is estimated to be 1300 MPa.
3. Clean metallurgical interfaces were observed between the CG and UFG Al 5083, and between the B_4C particles and the Al 5083 matrix.
4. The overall effect on strength of the microstructural features observed in this study were quantified by implementing three existing models, i.e., rule-of-mixtures, modified shear-lag and Mori–Tanaka, all of which indicate that most of the ultra-high strength observed in the tri-modal composite is accounted for by the strengthening mechanisms studied in this work. Additional work is necessary to account for impurities in the system and to better model, and therefore aggregate, the interactions between mechanisms.

Acknowledgements

The authors would like to acknowledge financial support from Army Research Laboratory Cooperative Agreement No: W911NF-08-2-0028. The authors also are grateful to Prof. S. P. Joshi, Department of Mechanical Engineering at National University of Singapore, for providing the algorithm for the M–T model and for useful technical discussions.

References

[1] V.C. Nardone, K.M. Prewo, Scr. Metall. 20 (1986) 43.
[2] T. Christman, A. Needleman, S. Suresh, Acta Metall. 37 (1989) 3029.
[3] T.W. Clyne, P.J. Withers, An Introduction to Metal Matrix Composites, Cambridge University Press, New York, 1993.
[4] S.G. Fishman, J. Metals 38 (1986) 26.
[5] Y. Flom, R.J. Arsenault, Mater. Sci. Eng. 77 (1986) 191.
[6] I.A. Ibrahim, F.A. Mohamed, E.J. Lavernia, J. Mater. Sci. 26 (1991) 1137.
[7] M.E. Smagorinski, P.G. Tsantrizos, S. Grenier, T. Brzezinski, G. Kim, Mater. Sci. Eng. A: Struct. Mater. Prop. Microstruct. Process. 244 (1998) 86.
[8] B.Q. Han, J.Y. Huang, Y.T. Zhu, E.J. Lavernia, Scr. Mater 54 (2006) 1175.
[9] M. Chauhan, I. Roy, F.A. Mohamed, Metall. Mater. Trans. A: Phys. Metall. Mater. Sci. 37A (2006) 2715.
[10] N.A. Krasilnikov, A. Sharafutdiniv, Mater. Sci. Eng. A: Struct. Mater. Prop. Microstruct. Process. 463 (2007) 74.
[11] Y.H. Zhao, X.Z. Liao, Z. Jin, R.Z. Valiev, Y.T. Zhu, Acta Mater. 52 (2004) 4589.
[12] C.C. Koch, D.G. Morris, K. Lu, A. Inoue, MRS Bull. 24 (1999) 54.
[13] E. Ma, Jom 58 (2006) 49.
[14] Y.T. Zhu, X.Z. Liao, Nat. Mater. 3 (2004) 351.
[15] V.L. Tellkamp, A. Melmed, E.J. Lavernia, Metall. Mater. Trans. A: Phys. Metall. Mater. Sci. 32 (2001) 2335.
[16] Y.M. Wang, M.W. Chen, F.H. Zhou, E. Ma, Nature 419 (2002) 912.
[17] Y.H. Zhao, T. Topping, J.F. Bingert, J.J. Thornton, A.M. Dangelewicz, Y. Li, W. Liu, Y.T. Zhu, Y.Z. Zhou, E.L. Lavernia, Adv. Mater. 20 (2008) 3028.
[18] K.X. Tao, H. Choo, H.Q. Li, B. Clausen, J.E. Jin, Y.K. Lee, Appl. Phys. Lett. 90 (2007) 3.
[19] L. Lu, Y.F. Shen, X.H. Chen, L.H. Qian, K. Lu, Science 304 (2004) 422.
[20] G. He, J. Eckert, W. Loser, L. Schultz, Nat. Mater. 2 (2003) 33.
[21] S. Cheng, Y.H. Zhao, Y.T. Zhu, E. Ma, Acta Mater. 55 (2007) 5822.
[22] D.J. Lloyd, Int. Mater. Rev. 39 (1994) 1.
[23] J. Ye, B.Q. Han, Z. Lee, B. Ahn, S.R. Nutt, J.M. Schoenung, Scr. Mater. 53 (2005) 481–486.
[24] W.A.J.F. Shackelford, J.S. Park, CRC Materials Science and Engineering Handbook, CRC Press, FL, Boca Raton, 2008.
[25] A.P. Newbery, S.R. Nutt, E.J. Lavernia, Jom 58 (2006) 56.
[26] J.M. Schoenung, J. Ye, J. He, F. Tang, D. Witkin, Mater. Forum 29 (2005) 123.
[27] H. Zhang, M.W. Chen, K.T. Ramesh, J. Ye, J.M. Schoenung, E.S.C. Chin, Mater. Sci. Eng. A: Struct. Mater. Prop. Microstruct. Process. 433 (2006) 70–82.

[28] R.G. Vogt, Z. Zhang, T.D. Topping, E.J. Lavernia, J.M. Schoenung, J. Mater. Process. Technol. 209 (2009) 5046.
[29] L.H. Dai, Z. Ling, Y.L. Bai, Compos. Sci. Technol. 61 (2001) 1057.
[30] H.L. Cox, Br. J. Appl. Phys. 3 (1952) 72.
[31] W.S. Miller, F.J. Humphreys, Scr. Metall. Mater. 25 (1991) 33.
[32] M.T. Marques, J.B. Correia, P. Matteazzi, Mater. Sci. Forum 455–456 (2004) 244.
[33] Z. Zhang, D.L. Chen, Scr. Mater. 54 (2006) 1321.
[34] Y.M. Wang, E. Ma, Acta Mater. 52 (2004) 1699.
[35] H.T. Zhang, J.C. Ye, S.P. Joshi, J.M. Schoenung, E.S.C. Chin, G.A. Gazonas, K.T. Ramesh, Adv. Eng. Mater. 9 (2007) 355.
[36] J.C. Ye, J.H. He, J.M. Schoenung, Metall. Mater. Trans. A: Phys. Metall. Mater. Sci. 37A (2006) 3099.
[37] J.C. Ye, Z. Lee, B. Ahn, J.H. He, S.R. Nutt, J.M. Schoenung, Metall. Mater. Trans. A: Phys. Metall. Mater. Sci. 37A (2006) 3111.
[38] N.D. Browning, M.F. Chisholm, S.J. Pennycook, Nature 366 (1993) 143.
[39] N.D. Browning, I. Arslan, Y. Ito, E.M. James, R.F. Klie, P. Moeck, T. Topuria, Y. Xin, J. Electron Microsc. 50 (2001) 205.
[40] G. Lucadamo, N.Y.C. Yang, C.S. Marchi, E.J. Lavernia, Mater. Sci. Eng. A: Struct. Mater. Prop. Microstruct. Process. 430 (2006) 230.
[41] C.Y. Yu, P.W. Kao, C.P. Chang, Acta Mater. 53 (2005) 4019.
[42] X.Z. Liao, J.Y. Huang, Y.T. Zhu, F. Zhou, E.J. Lavernia, Philos. Mag. 83 (2003) 3065.
[43] T. Ungar, J. Gubicza, G. Ribarik, A. Borbely, J. Appl. Crystallogr. 34 (2001) 298.
[44] F.S.M. Kocer, M. Muller, Nondestructive Characterization of Materials, vol. VII, 1996.
[45] R. Benedictus, A. Bottger, E.J. Mittemeijer, Phys. Rev. B 54 (1996) 9109.
[46] Y.W. Kim, W.M. Griffith, F.H. Froes, J. Metals 37 (1985) 27.
[47] E.O. Hall, Proc. Phys. Soc. Lond. Sect. B 64 (1951) 747.
[48] N.J. Petch, J. Iron Steel Inst. 174 (1953) 25.
[49] H.R. Last, R.K. Garrett, Metall. Mater. Trans. A: Phys. Metall. Mater. Sci. 27 (1996) 737.
[50] J.R. Davis, ASM Specialty Handbook—Aluminum and Aluminum Alloys, ASM International, OH, Materials Park, 1994.
[51] H.R.,L.M. Brown, Strengthening Methods in Crystals, Elsevier, Amsterdam, 1971.
[52] B.Q. Han, Z. Lee, S.R. Nutt, E.J. Lavernia, F.A. Mohamed, Metall. Mater. Trans. A: Phys. Metall. Mater. Sci. 34 (2002) 603.
[53] M.F. Ashby, Philos. Mag. 21 (1970) 399.
[54] N.A. Fleck, G.M. Muller, M.F. Ashby, J.W. Hutchinson, Acta Metall. Mater. 42 (1994) 475.
[55] A. Seeger, Moderne Problems der Metallphysik, Springer, 1985.
[56] V. Laws, J. Mater. Sci. Lett. 2 (1983) 527.
[57] L. He, L.F. Allard, E. Ma, Scr. Mater. 42 (2000) 517.
[58] H.S. Kim, Mater. Sci. Eng. A: Struct. Mater. Prop. Microstruct. Process. 289 (2000) 30.
[59] H.A. Bruck, B.H. Rabin, J. Mater. Sci. 34 (1999) 2241.
[60] A.L. Greer, Mater. Sci. Eng. A: Struct. Mater. Prop. Microstruct. Process. 304 (2001) 68.
[61] H.J. Edrees, A.C. Smith, A. Hendry, J. Eur. Ceram. Soc. 18 (1998) 275.
[62] V.C. Nardone, J.K. Tien, Scr. Metall. 20 (1986) 797.
[63] M.R. Piggot (Ed.), Load-Bearing Fibre Composites, Pergamon Press, New York, 1980.
[64] T.G. Nieh, J. Wadsworth, D.J. Chellmann, Scr. Metall. 19 (1985) 181.
[65] T. Mori, K. Tanaka, Acta Metall. 21 (1973) 571.
[66] G.J. Weng, J. Mech. Phys. Solids 38 (1990) 419.
[67] Y. Rudiono, Tomota, Acta Mater. 45 (1997) 1923.
[68] C.W. Nan, D.R. Clarke, Acta Mater. 44 (1996) 3801.
[69] S.P. Joshi, K.T. Ramesh, Scr. Mater. 57 (2007) 877.
[70] S.P. Joshi, K.T. Ramesh, B.Q. Han, E.J. Lavernia, Metall. Mater. Trans. A: Phys. Metall. Mater. Sci. 37A (2006) 2397.
[71] L.H. Sjodahl, J.B. Conway, Trans. Metall. Soc. Aime 245 (1969) 1659.
[72] E.Y. Gutmanas, Prog. Mater. Sci. 34 (1990) 261.
[73] M.J. Luton, C.S. Jayanth, M.M. Disko, S. Matras, J. Vallone, Proceedings of the MRS Symposium: Multicomponent Ultrafine Microstructures, Boston, 1988.
[74] L. Wang, N. Beck, R.J. Arsenault, Mater. Sci. Eng. A: Struct. Mater. Prop. Microstruct. Process. 177 (1994) 83.
[75] J.R. Scully, G.A. Young, S.W. Smith, Mater. Sci. Forum 331–337 (2000) 1583.